Computers in Biology and Medicine 41 (2011) 326–339

Contents lists available at ScienceDirect

Computers in Biology and Medicine

journal homepage: www.elsevier.com/locate/cbm

Segmentation of 3D cell membrane images by PDE methods and its applications

K. Mikula [a], N. Peyriéras [b], M. Remešíková [a,*], O. Stašová [a]

[a] Slovak University of Technology, Department of Mathematics, Radlinského 11, 81368 Bratislava, Slovakia
[b] CNRS-DEPSN, Avenue de la Terasse, 91198 Gif sur Yvette, France

ARTICLE INFO

Article history:
Received 4 May 2010
Accepted 24 March 2011

Keywords:
Cell image
Cell membranes
Segmentation
Object counting
Intercellular skeleton
Subjective surface method
Image processing
Partial differential equation

ABSTRACT

We present a set of techniques that enable us to segment objects from 3D cell membrane images. Particularly, we propose methods for detection of approximate cell nuclei centers, extraction of the inner cell boundaries, the surface of the organism and the intercellular borders—the so called intercellular skeleton. All methods are based on numerical solution of partial differential equations. The center detection problem is represented by a level set equation for advective motion in normal direction with curvature term. In case of the inner cell boundaries and the global surface, we use the generalized subjective surface model. The intercellular borders are segmented by the advective level set equation where the velocity field is given by the gradient of the signed distance function to the segmented inner cell boundaries. The distance function is computed by solving the time relaxed eikonal equation. We describe the mathematical models, explain their numerical approximation and finally we present various possible practical applications on the images of zebrafish embryogenesis—computation of important quantitative characteristics, evaluation of the cell shape, detection of cell divisions and others.

1. Introduction

Cell membrane is a fundamental structure of living organisms, from bacteria to humans, separating the interior of cells from the outside environment. Inspection of these membranes is necessary whenever we want to evaluate the shape of a cell or measure some quantities such as volume or contact surface with the neighboring cells. The modern biological and microscopy tools enable us to selectively stain the membrane structures and then perform the imaging that can vary from a single 2D image to long series of 3D images mapping the time evolution of an organism or its parts.

Although biologists have been so far mainly exploiting image data sets by manual analysis, 3D and 3D+time confocal microscopy imaging of entire living organisms produce huge amounts of data that can be properly analyzed only through automated procedures, using computers and appropriate image processing algorithms. While single 2D or 3D images can be sometimes processed using the most simple approaches, when dealing with long time sequences of data, the methods must be robust enough to handle the possible imperfections of the images – noise, artifacts, incomplete boundaries of objects, etc. Imaging the time evolution of an organism always requires some sort of compromise – maximizing the signal quality, minimizing the time interval between two subsequent images, taking in account the limited resistance of the living organism to the action of the technical device, etc. As a consequence, we must always expect a certain level of noise, spurious structures and other effects and any method applied to the images must be well adapted to such difficulties.

This paper suggests several mathematical and computational image processing techniques for treating the cell membrane images. We use 3D biphoton laser scanning microscopy images taken throughout early embryogenesis of zebrafish (*Danio rerio*) embryos. First, we show how we can segment the inner boundaries of all individual cells. We use a method based on numerical solution of a PDE model, the so called generalized subjective surface equation [6,14,13,16,22]. Then we show that the same strategy can be used to segment the global surface (in our case the surface of the part of the embryo visible in the image). Finally, we present a technique to construct the so called intercellular skeleton (cell contact surface). Here, we first compute the signed distance function to the segmented inner boundaries of the cells by solving the time relaxed eikonal equation. After, we apply the advective level set model with the velocity field given by the gradient of the computed distance function. As a result we obtain the ridges of the signed distance function that represent the

* Corresponding author. Tel.: +421 905919096.
E-mail addresses: mikula@math.sk (K. Mikula), nadine.peyrieras@inaf.cnrs-gif.fr (N. Peyriéras), remesikova@math.sk (M. Remešíková), stasova@math.sk (O. Stašová).

0010-4825/$ - see front matter © 2011 Elsevier Ltd. All rights reserved.
doi:10.1016/j.compbiomed.2011.03.010

desired intercellular skeleton. In order to perform all these segmentations automatically, we also need to automatically construct appropriate initial segmentation functions. In case of the cell border segmentation, the compact support of the initial function should be located in the neighborhood of the (approximate) cell center. Therefore, before we start explaining the segmentation techniques, we present a method for automatic cell nuclei center detection. This detection uses cell nuclei images that can be scanned simultaneously with the membranes, in the second channel of a confocal microscope.

Segmentation of cell nuclei and cell membrane images as well as the center detection problem was previously discussed e.g. in [1,9,13,22]. The methods presented in these works were successfully applied in practice and allowed us to obtain a number of results [1,2,5,12,22]. The extensive testing indicated both advantages and drawbacks of the proposed techniques, possibilities of their improvement and a large variety of further applications. The main goal of this paper is to apply different, more efficient numerical approaches, apply them to advanced analysis of embryogenesis image data and thus provide a complex, experience based explanation of processing and analysis of cell membrane images.

Speaking in detail, we provide here an improvement of the efficiency of the center detection algorithm introduced in [9]. This is achieved by applying the Rouy–Tourin approximation to the term representing the motion of level sets in normal direction. This modification leads to both CPU time improvement and better accuracy of the result. The solution of the subjective surface models was simplified by applying the upwind discretization of the advective terms. We would like to emphasize that the efficiency of the methods has to be viewed in the context of processing large datasets and a huge number of individual cells. Being aware of the practical difficulties and demands that such data bring, it is necessary to concentrate the research on finding the numerical methods as efficient as possible.

Another important improvement introduced in this paper concerns the detection of the intercellular skeleton. Contrarily to [2], we provide here a 3D method for the extraction of the skeleton, we apply it to a whole embryo, which involves also the embryo surface segmentation, we validate the technique and we mention and illustrate several practical applications, i.e determining the cell shapes and quantitative characteristics of the embryo or detection of the cell layers.

Together with these novel contributions, the paper also provides to the reader a synthesis of the cell membrane image processing methodology. Therefore it contains the full description of the corresponding set of mathematical models and a detailed explanation of the semi-implicit time discretization and the finite volume space discretization. To conclude, we provide a paper with a complete and transparent description of the membrane image processing chain, with the numerical methods that appeared to be the most efficient in practical experiments, in a way that would make the algorithms easy to understand and reproduce, with validation and a number of suggestions of practical applications.

The numerical approximations of the models are based on the following ideas. The time discretization of the time relaxed eikonal equation and the advective level set model is explicit while the center detection equation and generalized subjective surface model, since they contain nonlinear curvature terms, are discretized by the semi-implicit approach. As for the space discretization, the advective term in the subjective surface model and in the advective level set model is approximated by applying the upwind principle. The center detection equation and the eikonal equation contain the term that represents motion of level sets in normal direction. Here we apply the Rouy–Tourin scheme. The curvature term in the center detection and the generalized subjective surface model is discretized by the finite volume technique. The application of the semi-implicit time discretization to the generalized subjective surface equation represents an improvement with respect to [22] where the explicit approach was used. The semi-implicit method guarantees the unconditional stability of the curvature term and thus it allows larger time discretization steps. The Rouy–Tourin scheme can significantly improve the efficiency of the center detection method compared with [9] where the so called flux-based level set method [8] was applied. The numerous tests also confirmed that the upwind strategy provides results of sufficient quality and it represents a more simple alternative to the flux-based level set method in case of the subjective surface segmentation [1,13,14].

From the biological point of view, we provide a complex set of techniques for analysis of the cell images. The computer analysis can provide an insight that would be impossible to achieve by an eye inspection and allows us to perform various measurements and statistical evaluations. As we will show, the results of the segmentation algorithms together with the center detection method can provide a number of useful information about the individual cells or about the whole organism. The segmented inner boundaries of the cells can be used for example for computation of the inner volume of each cell or for detection of cell divisions. The global surface segmentation provides the information about the volume and surface of the whole organism, the local and global densities of cells, etc. The intercellular skeleton can be used to measure the cell contact surface, evaluate the shape of the cells, detect specific cell groups or layers. All these results can be further used for analysis of 4D data (the time evolution of an organism) or for comparison of different individuals. We provide several improvements and extensions with respect to the related works, e.g. [1,20,22]. We use the cell shape evaluation described in [20] but we inspect later stages of embryonic development with a much larger number of cells and different features. Contrarily to [22], we segment both inner and outer (intercellular) borders and the global surface. In addition to the applications mentioned in [1], we indicate e.g. how we can recognize the epiblast layers at gastrulation stages of embryogenesis or calculate some quantitative characteristics of the organism.

The paper has the following organization. First, we present the data we are dealing with and we briefly describe their preprocessing. Then we explain the methods—for each method, we first present the mathematical model and then we describe the numerical approximation. In the last section, we suggest some possible practical applications of the segmentation methods, we show some results obtained from the zebrafish embryogenesis images and we also provide a validation of the computed intercellular skeleton done by comparing with a manual segmentation.

2. Cell image data and image preprocessing

Our research was mainly focused on images representing the early embryonic development of zebrafish. This animal is a privileged model organism in developmental biology because its embryos are easily available, develop rapidly and are transparent. The images are obtained by a biphoton laser scanning microscopy with one detection channel corresponding to cell membranes. This one-color representation is equivalent to the greylevel scale, therefore we will consider our images to be represented by a scalar grey intensity function.

Let us denote by $u_M^0 : \Omega \to R$ the intensity function representing the cell membrane image, Ω being a 3D rectangular image domain. Without loss of generality we can assume that $0 \le u_M^0 \le 1$. Fig. 1 shows a typical example of such an image, in horizontal and vertical slice views. This image represents a part of

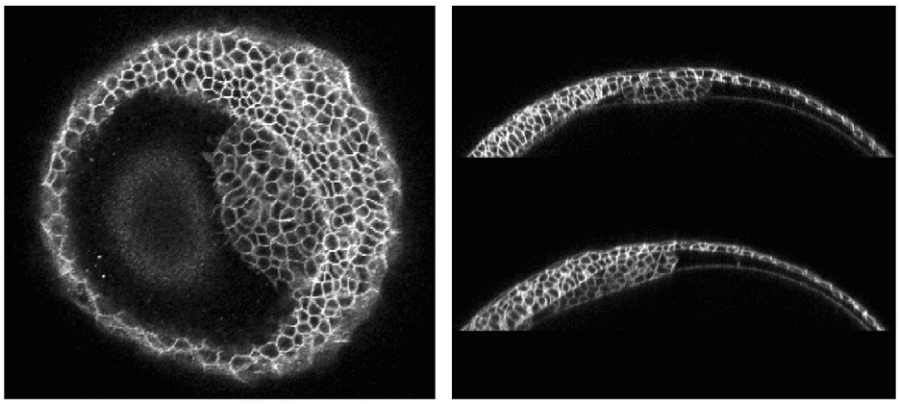

Fig. 1. The cell membrane images. Left, optical section corresponding to the *xy* scanned plane. Right, the *xz* slice, i.e. orthogonal to the imaging plane views.

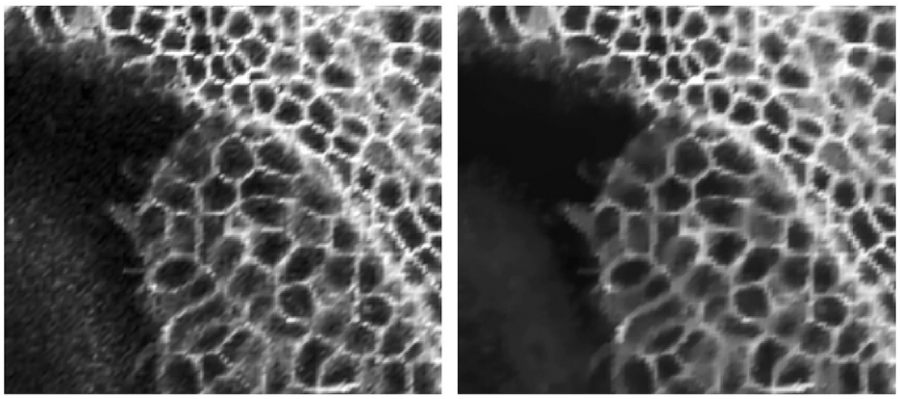

Fig. 2. An illustration of the data preprocessing (denoising). Left, a detail of the original image. Right, the filtered image.

an embryo (scanned from the animal pole) at the late gastrulation stage of embryonic development, the stage that precedes the formation of organs, and covers about ten thousand cells.

As we can see, the level of noise in these images is rather high, although we present data with a relatively slow pixel time rate (4.88 μs/pixel). It would be practically impossible to proceed without first removing the noise with an appropriate filtering algorithm. In our case, we used the so called geodesic mean curvature flow model [3,11,4], which was chosen from several possibilities after extensive testing [12]. Let $u^0_{M_f}$ denote the result of the filtering. An example is shown in Fig. 2 where we display a detail of original and filtered data.

3. Algorithms for the cell image processing

In this section, we describe several methods designed to extract information from cell membrane images. A necessary preliminary step for all these techniques is the detection of cell nuclei centers, therefore we start up by explaining a method that can be generally used for counting and locating the objects in various types of images. For each method, we first present the corresponding mathematical model and after we explain its numerical approximation. All techniques are presented in such a form that their implementation should be straightforward.

3.1. Detection of cell nuclei centers

In the process of the cell boundary segmentation, we want to work individually with each cell. For this purpose we first need to know the approximate position of the cell, i.e., the approximate position of its center. Though it might be difficult to obtain such centers from the cell membrane image, they can be successfully located using the cell nuclei image which is acquired simultaneously with the membrane image but in a separate channel [9,17].

The principle of the center detection algorithm, applicable to a general object counting and locating problem, is based on the following idea [9]. As we can see in Fig. 3, the cell nuclei image contains objects of relatively high intensity with respect to the background. Our goal is to locate the significant objects, i.e. the cell nuclei, and omit the spurious structures like noise, artifacts or local structures other than nuclei. This can be done if we realize that any object visible in the image is represented by certain image intensity level sets. All objects can then be classified according to the diameter of these level sets—level sets with a relatively large diameter, $0 \ll c_1 \le d \le c_2$, correspond to significant objects, while the ones with a small diameter, $0 < d \ll c_1$, can be identified as spurious structures.

In general, the level sets are closed surfaces. If we want to select the ones with large diameter, we simply let all their points move at a constant speed in the direction of the corresponding inner normal to the level set. Such a motion leads to shrinking and finally disappearing of the level set. During this process, the level sets with small diameter naturally disappear quickly whereas the ones with large diameter are observable in a much longer time scale. Therefore, if we choose an appropriate stopping time, the important objects are still present while the spurious ones have already disappeared.

In order to speed up the described advective level set motion, we take the normal velocity V of any level set in the form $V = \delta + \mu k$ where δ and μ are constants and k is the mean

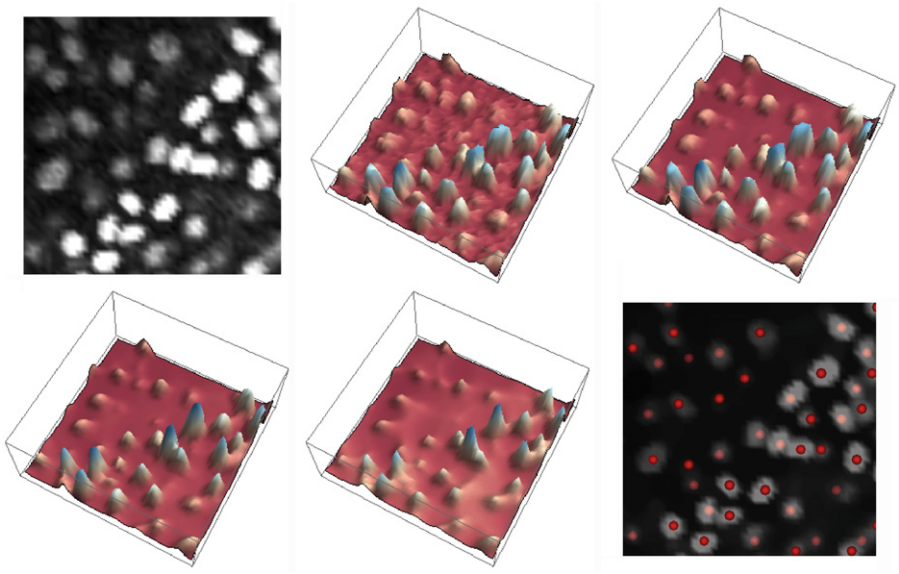

Fig. 3. Demonstration of the nuclei center detection process. Top left, 2D slice of the nuclei image. Top middle, plot of the corresponding intensity function. Top right, intensity function of the filtered data. Bottom left and middle, the intensity function after 5 and 15 steps of the evolution given by (1). Bottom right, 2D slice of filtered data and the corresponding centers constructed after five time steps of the evolution. This number of time steps was determined as optimal for the presented image.

curvature. Then we can model the level set evolution process as follows:

$$u_t - \delta|\nabla u| - \mu|\nabla u|\nabla\cdot\left(\frac{\nabla u}{|\nabla u|}\right)=0, \tag{1}$$

coupled with the zero Neumann boundary condition. The initial condition for this equation is $u_0 = u^0_{N_f}$ where $u^0_{N_f}$ is the filtered cell nuclei image. Similarly as in the case of cell membrane images, we used the GMCF filtering method.

Due to the shrinking and smoothing of all structures in the described evolution process, we observe decreasing of the number of local maxima of the solution u satisfying Eq. (1). This decrease is fast at the beginning and later it is stabilized. We stop this process when the slope of the decreasing is below a certain threshold. The approximate cell nuclei centers are represented by the points where the function u reaches its local maxima at the stopping time T_C. The principle of the center detection process is illustrated in Fig. 3.

Now let us explain the discretization of the model (1). Let N_C be the number of time steps and $\tau_C = T_C/N_C$ the corresponding uniform time step. We consider the following semi-implicit time discretization:

$$\frac{u^n-u^{n-1}}{\tau_C} - \delta|\nabla u^{n-1}| - \mu|\nabla u^{n-1}|\nabla\cdot\left(\frac{\nabla u^n}{|\nabla u^{n-1}|}\right)=0, \tag{2}$$

for any $n=1,\ldots,N_C$. This type of time discretization guarantees the unconditional stability of the curvature term.

In order to perform the space discretization, we apply the finite volume strategy where the finite volumes of the mesh $\mathcal{T}_h$ are identified with the voxels of the 3D image. Let us suppose that any volume (voxel) V_{ijk}, $i=1,\ldots,N_1$, $j=1,\ldots,N_2$, $k=1,\ldots,N_3$, is represented by a cube with side length h. Let $m(V_{ijk})$ denote the volume of V_{ijk} and c_{ijk} its barycenter. By u^n_{ijk} we will denote the approximate value of u^n in c_{ijk} (Fig. 4).

For all volumes V_{ijk}, we define two index sets. First, let N_{ijk} denote the set of all (p,q,r) such that $p,q,r\in\{-1,0,1\}$, $|p|+|q|+|r|=1$. Then, let P_{ijk} represent the set of all (p,q,r) satisfying $p,q,r\in\{-1,0,1\}$, $|p|+|q|+|r|=2$. Let us first consider $(p,q,r)\in N_{ijk}$. The line connecting the center of V_{ijk} and the center of its neighbor $V_{i+p,j+q,k+r}$ is denoted by s^{pqr}_{ijk} and its length by $m(s^{pqr}_{ijk})$. The faces of the finite volume V_{ijk} are denoted by e^{pqr}_{ijk} with

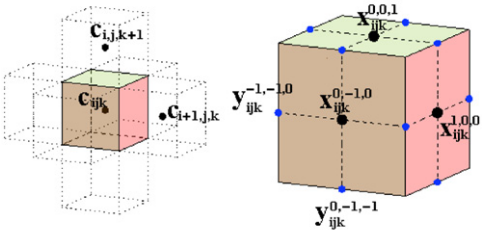

Fig. 4. The finite volume mesh.

area $m(e^{pqr}_{ijk})$ and normal ν^{pqr}_{ijk}. Let x^{pqr}_{ijk} be the point where the line s^{pqr}_{ijk} crosses the face e^{pqr}_{ijk}. Finally, for any $(p,q,r)\in P_{ijk}$, let y^{pqr}_{ijk} denote the midpoints of the voxel edges. The approximate value of u^{n-1} at x^{pqr}_{ijk} and y^{pqr}_{ijk}, where (p,q,r) belongs to the corresponding index set, is denoted by u^{pqr}_{ijk}, omitting the time index, as only the values from the time level $n-1$ will be needed in these points.

In order to implement the Neumann boundary condition, we use the reflection principle, i.e. we consider additional volumes with indices $i=0$, $i=N_1+1$, $j=0$, $j=N_2+1$, $k=0$, $k=N_3+1$ and we set $u^n_{0jk}=u^n_{2jk}$ for all $j=1,\ldots,N_2$, $k=1,\ldots,N_3$ and analogously for the other domain boundaries.

Now let us integrate (2) over the finite volume V_{ijk}. We get

$$\int_{V_{ijk}}\frac{u^n-u^{n-1}}{\tau_C}dx - \int_{V_{ijk}}\delta|\nabla u^{n-1}|dx - \int_{V_{ijk}}\mu|\nabla u^{n-1}|\nabla\cdot\left(\frac{\nabla u^n}{|\nabla u^{n-1}|}\right)dx=0. \tag{3}$$

The time derivative term can be approximated straightforwardly:

$$\int_{V_{ijk}}\frac{u^n-u^{n-1}}{\tau_C}dx \approx m(V_{ijk})\frac{u^n_{ijk}-u^{n-1}_{ijk}}{\tau_C} \tag{4}$$

and now we explain in details the approximation of the other two terms on the LHS of (3).

The second term contains the absolute value of the gradient $|\nabla u^{n-1}|$. A good quality approximation of this expression is provided by the Rouy–Tourin scheme [15]. Let us define for any $(p,q,r)\in N_{ijk}$:

$$D^{pqr}_{ijk} = (\min(u^{n-1}_{i+p,j+q,k+r}-u^{n-1}_{ijk},0))^2 \tag{5}$$

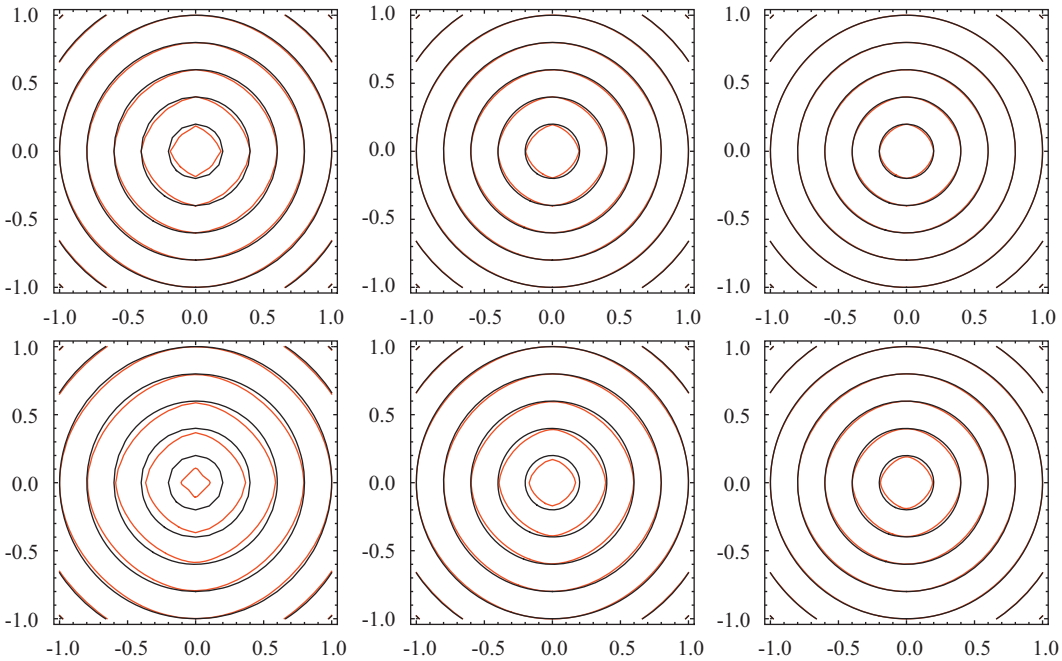

Fig. 5. Solution of Eq. (13) obtained by the Rouy–Tourin scheme (top) and the flux-based level set method (bottom). We display results for $h=0.1$ (left), $h=0.05$ (middle) and $h=0.025$ (right). The images are contour plots of the exact (black) and numerical solution (red), the innermost circle represents the zero level set. (For interpretation of the references to color in this figure legend, the reader is referred to the web version of this article.)

and further

$$M_{ijk}^{100}=\max(D_{ijk}^{-1,0,0},D_{ijk}^{1,0,0}),\quad M_{ijk}^{010}=\max(D_{ijk}^{0,-1,0},D_{ijk}^{0,1,0}),$$

$$M_{ijk}^{001}=\max(D_{ijk}^{0,0,-1},D_{ijk}^{0,0,1}) \tag{6}$$

Then we get the approximations

$$|\nabla u^{n-1}|\approx\frac{1}{h}\sqrt{M_{ijk}^{100}+M_{ijk}^{010}+M_{ijk}^{001}} \tag{7}$$

$$\int_{V_{ijk}}\delta|\nabla u^{n-1}|dx\approx\frac{\delta m(V_{ijk})}{h}\sqrt{M_{ijk}^{100}+M_{ijk}^{010}+M_{ijk}^{001}}. \tag{8}$$

The integral of the curvature term in (3) can be rewritten as follows:

$$\int_{V_{ijk}}\mu|\nabla u^{n-1}|\nabla\cdot\left(\frac{\nabla u^n}{|\nabla u^{n-1}|}\right)dx=\mu\overline{Q}_{ijk}^{n-1}\sum_{N_{ijk}}\int_{e_{ijk}^{pqr}}\frac{\nabla u^n}{|\nabla u^{n-1}|}v_{ijk}^{pqr}\,d\gamma, \tag{9}$$

where $\overline{Q}_{ijk}^{n-1}$ is an average modulus of $|\nabla u^{n-1}|$ in V_{ijk}. To complete the discretization, we need to approximate $\overline{Q}_{ijk}^{n-1}$ and its equivalent $Q_{ijk}^{pqr;n-1}$—the average modulus of $|\nabla u^{n-1}|$ on the voxel faces e_{ijk}^{pqr}. Let us note that in practical implementations the absolute value of gradient $|\nabla u^{n-1}|$ in the curvature term, since it appears in denominator, is substituted by the regularized term $\sqrt{\varepsilon^2+|\nabla u^{n-1}|^2}$. Then instead of $\overline{Q}_{ijk}^{n-1}$, $Q_{ijk}^{pqr;n-1}$ we use their regularized equivalents $\overline{Q}_{\varepsilon;ijk}^{n-1}$, $Q_{\varepsilon;ijk}^{pqr;n-1}$.

Now let us consider the midpoints y_{ijk}^{pqr}, $(p,q,r)\in P_{ijk}$, of the voxel edges. The values of u^{n-1} in these points can be approximated as

$$u_{ijk}^{pq0}=\tfrac{1}{4}(u_{ijk}^{n-1}+u_{i+p,j,k}^{n-1}+u_{i,j+q,k}^{n-1}+u_{i+p,j+q,k}^{n-1}),$$

$$u_{ijk}^{p0r}=\tfrac{1}{4}(u_{ijk}^{n-1}+u_{i+p,j,k}^{n-1}+u_{i,j,k+r}^{n-1}+u_{i+p,j,k+r}^{n-1}),$$

$$u_{ijk}^{0qr}=\tfrac{1}{4}(u_{ijk}^{n-1}+u_{i,j+q,k}^{n-1}+u_{i,j,k+r}^{n-1}+u_{i,j+q,k+r}^{n-1}).$$

Let us denote by $\nabla^{pqr}u_{ijk}^{n-1}$ the approximation of the gradient in the barycenter x_{ijk}^{pqr} of the face e_{ijk}^{pqr}, $(p,q,r)\in N_{ijk}$, of the voxel V_{ijk}. Using this notation, we can define

$$\nabla^{p00}u_{ijk}^{n-1}=(p(u_{i+p,j,k}^{n-1}-u_{ijk}^{n-1})/h,\,(u_{ijk}^{p10}-u_{ijk}^{p,-1,0})/h,\,(u_{ijk}^{p01}-u_{ijk}^{p,0,-1})/h),$$

$$\nabla^{0q0}u_{ijk}^{n-1}=((u_{ijk}^{1q0}-u_{ijk}^{-1,q,0})/h,\,q(u_{i,j+q,k}^{n-1}-u_{ijk}^{n-1})/h,\,(u_{ijk}^{0q1}-u_{ijk}^{0,q,-1})/h),$$

$$\nabla^{00r}u_{ijk}^{n-1}=((u_{ijk}^{10r}-u_{ijk}^{-1,0,r})/h,\,(u_{ijk}^{01r}-u_{ijk}^{0,-1,r})/h,\,r(u_{i,j,k+r}^{n-1}-u_{ijk}^{n-1})/h).$$

The required approximations can be now defined as

$$Q_{ijk}^{pqr;n-1}=|\nabla^{pqr}u_{ijk}^{n-1}|,\quad Q_{\varepsilon,ijk}^{pqr;n-1}=\sqrt{\varepsilon^2+|\nabla^{pqr}u_{ijk}^{n-1}|^2},$$

$$\overline{Q}_{ijk}^{n-1}=\frac{1}{6}\sum_{N_{ijk}}|\nabla^{pqr}u_{ijk}^{n-1}|,\quad \overline{Q}_{\varepsilon,ijk}^{n-1}=\sqrt{\varepsilon^2+\frac{1}{6}\sum_{N_{ijk}}|\nabla^{pqr}u_{ijk}^{n-1}|^2} \tag{10}$$

and we can complete the approximation of (9):

$$\int_{V_{ijk}}\mu|\nabla u^{n-1}|\nabla\cdot\left(\frac{\nabla u^n}{|\nabla u^{n-1}|}\right)dx\approx\mu\overline{Q}_{ijk}^{n-1}\sum_{N_{ijk}}\frac{m(e_{ijk}^{pqr})}{m(s_{ijk}^{pqr})}\frac{u_{i+p,j+q,k+r}^{n}-u_{ijk}^{n}}{Q_{ijk}^{pqr;n-1}}. \tag{11}$$

Let us mention that the technique described above was tested in [14] together with other methods based on similar principles. Among the examined methods, this type of discretization appeared to be the most suitable for practical purposes due to its simplicity and overall good performance.

Finally, we can write the fully discrete formulation of the center detection equation (1). Summarizing the approximations (4), (8) and (11), realizing that $m(V_{ijk})=h^3$, $m(e_{ijk}^{pqr})=h^2$, $m(s_{ijk}^{pqr})=h$ and denoting the space step h for the center detection problem by h_C we get

$$\left(1+\mu\frac{\tau_C}{h_C^2}\sum_{N_{ijk}}\frac{\overline{Q}_{ijk}^{n-1}}{Q_{ijk}^{pqr;n-1}}\right)u_{ijk}^{n}-\mu\frac{\tau_C}{h_C^2}\sum_{N_{ijk}}\frac{\overline{Q}_{ijk}^{n-1}}{Q_{ijk}^{pqr;n-1}}u_{i+p,j+q,k+r}^{n}$$

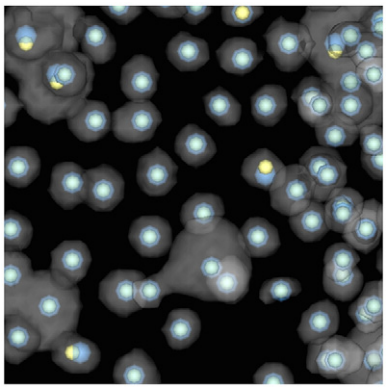

Fig. 6. Nuclei centers obtained with flux-based level set method (larger spheres) and Rouy–Tourin discretization (small spheres) applied to (1).

Table 1
Comparison of the flux-based level set method and the Rouy–Tourin discretization applied to (13).

h	τ R–T	τ FBLSM	$L_2(\Omega)$*error* R–T	$L_2(\Omega)$*error* FBLSM
0.1	0.05	0.025	2.667512e−2	6.581266e−2
0.05	0.025	0.0125	1.502070e−2	3.273901e−2
0.025	0.0125	0.00625	7.969409e−3	1.650439e−2

Table 2
Comparison of the flux-based level set method and Rouy–Tourin discretization applied to (1).

Method	τ_C	Time steps	Centers	*CPU* (s)
FBLSM	0.00125	4	8670	314.77
R-T	0.0025	3	8647	202.23

$$= u_{ijk}^{n-1} + \delta \frac{\tau_C}{h_C} \sqrt{M_{ijk}^{100} + M_{ijk}^{010} + M_{ijk}^{001}}. \tag{12}$$

At the end, we present two experiments illustrating the advantages of the Rouy–Tourin approximation in order to clarify our motivation for using this scheme. In [9], contrarily to this paper, the so called flux-based level set (FBLS) technique was applied in order to discretize (1). Figs. 5 and 6 together with Tables 1 and 2 show the comparison of the two methods. The first experiment is a 2D test example where we solve the following equation:

$$u_t - |\nabla u| = 0, \tag{13}$$

on the domain $[-1,1]\times[-1,1]$ with the initial condition

$$u_0(x,y) = \sqrt{x^2+y^2} - 0.95$$

and the boundary condition

$$u(x,y,t) = F(x,y,t) \quad \forall (x,y) \in \partial\Omega,$$

where

$$F(x,y,t) = u_0(x,y) + t$$

is the exact solution of Eq. (13) representing shrinking of circular level sets of the function u at a constant speed $v=1$. Fig. 5 shows the results for three different space discretization steps at time $T=0.75$. As we can see, the Rouy–Tourin scheme provides more precise results. This visual inspection is verified by Table 1 that shows the error of the numerical solutions corresponding to the pictures. Another advantage of the Rouy–Tourin scheme is that in general, it is stable (in 2D) if $\tau \le h/2$, where τ and h are the time and space discretization steps, while the basic flux-based level set method requires $\tau \le h/4$. Therefore, the Rouy–Tourin scheme allows larger time steps which leads to shorter CPU time needed for the computation.

The second experiment is a practical example where we detect cell nuclei centers in a selected subvolume of a 3D image. As we can see in Fig. 6, the quality of the results obtained by the two methods is very similar—the positions of the detected centers only slightly differ in some cases and the difference in the number of detected centers is less than 0.3% of the total number of centers. The difference is in the efficiency of the methods (Table 2)—since the Rouy–Tourin discretization allows us to use larger time steps, the total CPU time is significantly shorter. To conclude, applying the Rouy–Tourin scheme, we gain in both performance and accuracy of the results. In addition, the Rouy–Tourin scheme is also more simple to implement.

3.2. Segmentation of the inner cell boundaries

As we can see e.g. in Fig. 1, the cell membranes have a certain nonnegligible thickness which means that we can distinguish between the inner and outer boundaries of the cell. If we consider the simplifying assumption that the cells are attached to each other, the outer boundary is equivalent to the intercellular border. Let us first describe the extraction of the inner boundary of the cell which will be later used as the basic step for obtaining the intercellular skeleton.

Let us assume that s_l, $l=1,\ldots,n_C$, are the points in R^3 where the approximate cell centers were detected by the center detection method. In order to segment the inner boundaries of the cells, we construct an initial segmentation function for any of these points. The compact support of any such function should be situated inside its respective cell. After, we let the function evolve by solving the following generalized subjective surface (GSUBSURF) equation [6,14,13,16,22]:

$$u_t - w_a \nabla g \cdot \nabla u - w_d g |\nabla u| \nabla \cdot \left(\frac{\nabla u}{|\nabla u|} \right) = 0, \tag{14}$$

where u is the evolving function, $u(0,x) = u_0(x)$ (the initial segmentation function) and we consider the zero Dirichlet boundary condition on $\partial\Omega$. The function g is the so called edge detector and it is of the form:

$$g(s) = \frac{1}{1+Ks^2}, \quad K \ge 0. \tag{15}$$

It is applied to the gradient of the filtered image additionally smoothed by the Gaussian kernel with a small variance σ ($g = g(|\nabla u_\sigma^0|)$, $u_\sigma^0 = G_\sigma * u_{M_f}^0$). The essential property of this function is that its negative gradient points towards the edges in the image.

The model (14) is a generalization of the subjective surface method introduced in [16] where the authors use the following model:

$$u_t - |\nabla u| \nabla \cdot \left(g \frac{\nabla u}{|\nabla u|} \right) = 0.$$

This equation is equivalent to (14) if we set $w_a = 1.0$ and $w_d = 1.0$. By introducing the new parameters w_a and w_d that can be seen as weights for the advection and diffusion processes, we obtain a more general and more flexible model. Having the possibility to control separately the two processes, we have the potential to improve the efficiency of the method, cf. [1].

The time discretization of the GSUBSURF equation is semi-implicit as in the case of the center detection problem. Let us suppose that we solve the equation in the time interval $[0,T_S]$ and let N_S be the corresponding number of uniform time steps and the

time step $\tau_S = T_S/N_S$. Then for all $n = 1,\ldots,N_S$ we get

$$\frac{u^n - u^{n-1}}{\tau_S} - w_a \nabla g \cdot \nabla u^{n-1} - w_d g |\nabla u^{n-1}| \nabla \cdot \frac{\nabla u^n}{|\nabla u^{n-1}|} = 0. \tag{16}$$

For the space discretization we use the finite volume mesh and the corresponding notation described in Section 3.1. The Dirichlet boundary condition is implemented by setting $u^n_{ijk} = 0$ for the volumes touching the boundary of the domain and all corresponding definitions and further steps are then valid only for the inner volumes V_{ijk}. Integrating (16) over the volume V_{ijk} we obtain

$$\int_{V_{ijk}} \frac{u^n - u^{n-1}}{\tau_S} dx - \int_{V_{ijk}} w_a \nabla g \cdot \nabla u^{n-1}\, dx - \int_{V_{ijk}} w_d g |\nabla u^{n-1}| \nabla \cdot \frac{\nabla u^n}{|\nabla u^{n-1}|} dx = 0 \tag{17}$$

and the time derivative term is again approximated by

$$\int_{V_{ijk}} \frac{u^n - u^{n-1}}{\tau_S} dx \approx m(V_{ijk}) \frac{u^n_{ijk} - u^{n-1}_{ijk}}{\tau_S}.$$

In order to discretize the other two terms, we have to approximate the average modulus of $g = g(|\nabla u^0_\sigma|)$. Using the definitions stated in Section 3.1, we can define

$$g_{ijk} = g\left(\frac{1}{6}\sum_{N_{ijk}} |\nabla^{pqr} u^0_{\sigma;ijk}|\right).$$

Now we can approximate the advection term in (17). For that purpose, we define the index set $I_{ijk} = \{(1,0,0),(0,1,0),(0,0,1)\}$ and the following central differences for all $(p,q,r) \in I_{ijk}$:

$$D^{pqr}_{ijk} g = (g_{i+p,j+q,k+r} - g_{i-p,j-q,k-r})/(2h). \tag{18}$$

Then we apply the upwind principle and we get

$$\int_{V_{ijk}} (-w_a \nabla g \cdot \nabla u) dx \approx w_a m(V_{ijk}) \sum_{I_{ijk}} \left(\max(-D^{pqr}_{ijk} g, 0) \frac{u^{n-1}_{ijk} - u^{n-1}_{i-p,j-q,k-r}}{m(s^{-p,-q,-r}_{ijk})} + \min(-D^{pqr}_{ijk} g, 0) \frac{u^{n-1}_{i+p,j+q,k+r} - u^{n-1}_{ijk}}{m(s^{pqr}_{ijk})} \right). \tag{19}$$

The diffusion term can be approximated similarly as in the case of the center detection, according to (11)

$$\int_{V_{ijk}} w_d g |\nabla u^{n-1}| \nabla \cdot \left(\frac{\nabla u^n}{|\nabla u^{n-1}|}\right) dx \approx w_d g_{ijk} \overline{Q}^{n-1}_{ijk} \sum_{N_{ijk}} \frac{m(e^{pqr}_{ijk})}{m(s^{pqr}_{ijk})} \frac{u^n_{i+p,j+q,k+r} - u^n_{ijk}}{Q^{pqr;n-1}_{ijk}}. \tag{20}$$

Now if we set $h = h_S$, we can write the fully discrete form of the GSUBSURF equation (14)

$$\left(1 + w_d g_{ijk} \frac{\tau_S}{h_S^2} \sum_{N_{ijk}} \frac{\overline{Q}^{n-1}_{ijk}}{Q^{pqr;n-1}_{ijk}}\right) u^n_{ijk} - w_d g_{ijk} \frac{\tau_S}{h_S^2} \sum_{N_{ijk}} \frac{\overline{Q}^{n-1}_{ijk}}{Q^{pqr;n-1}_{ijk}} u^n_{i+p,j+q,k+r} = u^{n-1}_{ijk} - w_a \frac{\tau_S}{h_S} \sum_{I_{ijk}} (\max(-D^{pqr}_{ijk} g, 0)(u^{n-1}_{ijk} - u^{n-1}_{i-p,j-q,k-r}) + \min(-D^{pqr}_{ijk} g, 0)(u^{n-1}_{i+p,j+q,k+r} - u^{n-1}_{ijk})). \tag{21}$$

3.3. The global surface segmentation

The model (14) is a powerful segmentation tool that can be used to extract objects from various images, e.g., in case of embryogenesis images, the cell nuclei or cell structures [1,7]. The cell membrane images can be used to segment not only the individual cells but also the surface of the whole embryo, respectively, the part of the embryo visible in the image. In this case, Eq. (14) is applied without change, the only thing that has to change is the initial segmentation function. As we have mentioned above, in case of a single cell segmentation, the compact support of the initial segmentation function should be situated in the neighborhood of the approximate cell center. In case of embryo segmentation, the compact support of the initial segmentation function should cover the whole embryo. Then, as the function is evolving according to (14) with the edge detector (15), its isosurfaces are attracted to the nearest edge—the border of the embryo.

3.4. Extraction of the intercellular skeleton

As we have already mentioned, the starting point for extraction of the intercellular skeleton is the segmentation of the inner boundaries of the cells obtained by the GSUBSURF segmentation. The procedure consists of two steps. The first step is the computation of the signed distance function to the segmented inner borders. In the second step, the gradient of the computed signed distance function is used to construct the vector field for the advection part of the subjective surface segmentation model. This segmentation extracts the ridges of the signed distance functions that represent the intercellular borders.

3.4.1. Computation of the signed distance function

Let us denote by Ω_0 the set of curves representing the inner cell borders. The distance function can be computed in several ways, analytically or by using some numerical method, cf. e.g. [19,24]. Within the scope of our research, we tested extensively the application of the eikonal equation with time relaxation (cf. [2]) that reads as follows:

$$d_t + |\nabla d| = 1. \tag{22}$$

The equation is solved in the domain $\Omega \times [0,T_D]$ where Ω is the image domain and it is coupled with a Dirichlet type condition:

$$d(x,t) = 0, \quad x \in \Omega_0 \subset \Omega. \tag{23}$$

By the problem formulated in this way the solution d approaches, as time is evolving, the distance function to the set Ω_0. The signed distance function $d^{\pm}$ can be constructed straightforwardly, since the result of the cell segmentation is a level set function. Choosing one of the level sets to represent the inner boundary of the cell, we are able to recognize the inner and outer parts of the cell. Then we set $d^{\pm} = -d$ inside the cell and $d^{\pm} = d$ outside.

In order to construct the numerical approximation of (22), we recall the center detection problem. We can see that (22) has a similar structure as the center detection model (1) with the difference that $\delta = -1$ and the curvature term is replaced by a constant $f = 1$. Therefore we can again apply the Rouy–Tourin scheme and the notation and approximations stated in (5)–(7) where we substitute d for u. Considering τ_D the time step and h_D the space step of the discretization, we obtain the discrete equation:

$$d^n_{ijk} = d^{n-1}_{ijk} + \tau_D - \frac{\tau_D}{h_D} \sqrt{M^{100}_{ijk} + M^{010}_{ijk} + M^{001}_{ijk}}. \tag{24}$$

This scheme is stable for $\tau_D \le h_D/3$ and it produces monotonically increasing updates that are gradually approaching a steady state—the approximation of the distance function. Due to this property, we can implement (24) in a computationally efficient way. Let us consider the index set $\mathcal{I}$ of all indices (i,j,k) and the set $\mathcal{F}^n$ that contains the indices $(i,j,k) \in \mathcal{I}$ of the volumes

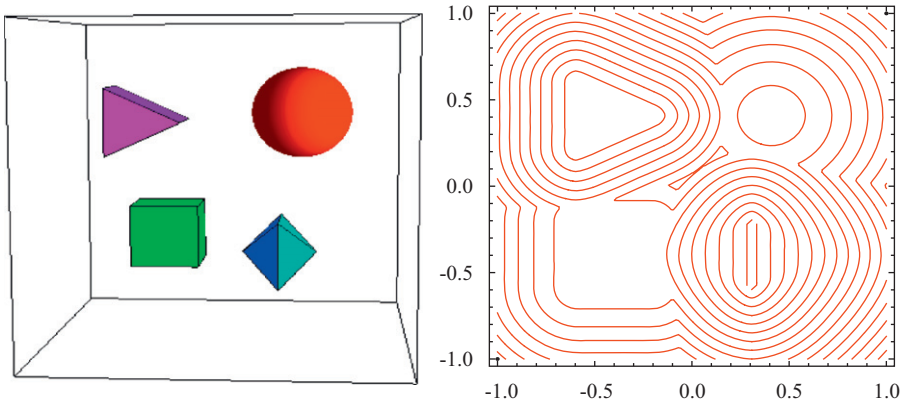

Fig. 7. Computation of the signed distance function to four 3D geometrical shapes. Right, a 2D cut of the contour plot of the distance function.

Table 3
Computational tests for the method without fixing in 3D—the distance function to four geometrical shapes.

n_x	τ_D	Time steps	$L_2(\Omega)$-error	CPU	EOC
25	$0.02\bar{6}$	118	8.195605e−2	0.16	
50	$0.01\bar{3}$	189	5.459197e−2	2.07	0.58616
100	$0.00\bar{6}$	320	3.398842e−2	25.66	0.68365
200	$0.00\bar{3}$	563	2.082350e−2	340.68	0.70683
400	$0.001\bar{6}$	390	1.244441e−2	5100	0.74272

Table 4
Computational tests for the method with fixing in 3D—the distance function to four geometrical shapes.

n_x	τ_D	Time steps	$L_2(\Omega)$-error	CPU	EOC
25	$0.02\bar{6}$	118	8.195604e−2	0.11	
50	$0.01\bar{3}$	189	5.459197e−2	1.37	0.58616
100	$0.00\bar{6}$	320	3.398842e−2	15.64	0.68365
200	$0.00\bar{3}$	563	2.082349e−2	206.54	0.70683
400	$0.001\bar{6}$	390	1.244439e−2	2820	0.74272

where the steady state has been already reached, i.e. there exists such $n_0 \in N$, $n_0 \le n$, that $d_{ijk}^{n_0} = d_{ijk}^{n_0-1}$. The set $\mathcal{F}^0$ is given as follows. Let us denote by Ω_1 the union of the set Ω_0 (the set of curves representing the segmented inner boundaries of cells) with its local (one voxel) neighborhood. At the beginning, we compute exact distances to the set Ω_0 in all voxels of Ω_1. Then $\mathcal{F}^0 = \Omega_1$ and the method is given by Algorithm 1. The basic principle is that we perform all computations only in the voxels that have not yet reached the steady state. The number of these voxels and the computational time needed to complete one time step of the procedure gradually decrease until the values in all voxels are fixed.

Algorithm 1. Fixing method for distance function.

- Set d_{ijk}^0 to values of the exact solution for all $(i,j,k) \in \Omega_1$
- $n=1$, $\mathcal{F}^0 = \Omega_1$
- **Do while** $\mathcal{F}^{n-1} \neq \mathcal{I}$
- Do **for all** $(i,j,k) \in \mathcal{I}$
- **if** $(i,j,k) \in \mathcal{F}^{n-1}$ **then** continue
- **else**
- $d_{ijk}^n = d_{ijk}^{n-1} + \tau_D - \frac{\tau_D}{h_D}\sqrt{M_{ijk}^{100} + M_{ijk}^{010} + M_{ijk}^{001}}$
- **if** $d_{ijk}^n = d_{ijk}^{n-1}$ **then** $\mathcal{F}^n = \mathcal{F}^{n-1} \cup \{(i,j,k)\}$
- $n=n+1$

Let us now perform a test experiment to determine the experimental order of convergence of the presented scheme and verify the validity of the fixing strategy. Let us consider a problem of computation of the distance function to four 3D geometrical shapes as displayed in Fig. 7. These shapes are located in a rectangular domain $\Omega = [-1,1]^3$. Table 3 shows the EOC, $L_\infty(I,L_2(\Omega))$ error and CPU time for the basic numerical (24). After, we provide Table 4 that shows the results obtained by the implementation represented by Algorithm 1. As we can see, the fixing strategy provides a significant reduction of the necessary computational time. Let us note that when the fixing is not applied, the computation is stopped when $\|d^{n+1} - d^n\|_{L_1\Omega} \le \varepsilon_1 \ll 1$ or when a prescribed number of time steps is completed. In our case, we prescribe exactly the same number of time steps that were needed to fix all values by the fixing strategy. In practical implementation, a value is fixed when $|d_{ijk}^{n+1} - d_{ijk}^n| \le \varepsilon_2 \ll 1$.

Remark 1. The efficiency of the presented method can be significantly improved if we realize the following fact. In order to segment the intercellular boundaries by the advective level set model, we do not necessarily need the exact distance function, the important factor is the correct orientation of the vector field given by the gradient of $d^{\pm}$ and the correct position of its ridges. As it follows from the character of the problem and also from the numerical procedure, a sufficient result is obtained as soon as the values in all image voxels are nontrivially updated by the numerical (24), i.e. before they are definitely fixed. Thus, the computational time can be considerably reduced while the quality of the result is preserved, cf [2] for a demonstration.

3.4.2. *Advective level set segmentation*

As we have already mentioned, the intercellular borders correspond to the ridges of the signed distance function. These ridges could be extracted by the GSUBSURF segmentation described in Section 3.2 with the signed distance function d (or a function depending on it) playing the role of the edge detector g. Since the velocity field given by the gradient of d does not induce any difficulties that are usually present in the scanned images (noise, spurious structures, incomplete borders), a simple advective level set model is sufficient, i.e., we solve the equation:

$$u_t + \nabla g \cdot \nabla u = 0, \tag{25}$$

where $(x,t) \in \Omega \times [0,T_A]$ and $g(x) = (d^{\pm}(x,T_D))^p$ according to [25] or $g(x) = -1/(1+K(d^{\pm}(x,T_D))^p)$ with $K>0$, $p>0$ as in [16,13]. The unknown function u is initialized by a piecewise constant profile localized around the approximate cell center. Then it is evolved by (25). Due to the properties of the function d, the isosurfaces of the evolving function u are attracted to the ridges of the distance

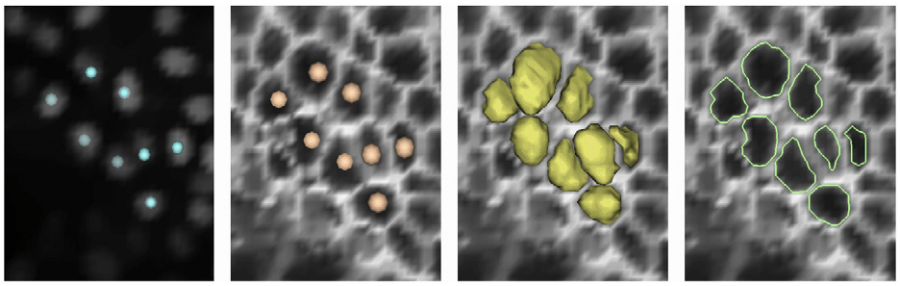

Fig. 8. Segmentation of the inner cell boundaries. From the left: 2D slice of the corresponding cell nuclei image with detected centers, 2D slice of the cell membrane image with an isosurface of the initial segmentation function, segmentation results (isosurface $I=128$ of the segmentation function), 2D slice of the segmentation results.

function and at the end they are attached to the borders of the neighboring cells. The outer boundary of the cell is then represented by a chosen level set of the function $u(x,T_A)$. For the epithelial cell layer that covers the embryo as well as the cell layer adjacent to the yolk cell, there is no ridge to stop the evolution of the function u in the parts where there are no neighboring cells (the apical surface of the cell). In this case, we use the segmented surface of the embryo to complete the missing boundary. Finally, the intercellular skeleton is formed by the union of all segmented outer cell boundaries.

Eq. (25) is discretized using the explicit time approach and upwind strategy given by (18) and (19). We can write

$$u_{ijk}^{n} = u_{ijk}^{n-1} - \frac{\tau_A}{h_A}\sum_{I_{ijk}}\Big(\max(D_{ijk}^{pqr}g,0)(u_{ijk}^{n-1}-u_{i-p,j-q,k-r}^{n-1}) + \min(D_{ijk}^{pqr}g,0)(u_{i+p,j+q,k+r}^{n-1}-u_{ijk}^{n-1})\Big), \tag{26}$$

where τ_A and h_A are the corresponding time and space steps.

4. Experiments and practical applications

4.1. Segmentation of the inner cell boundaries

The first result that we present is the extraction of the inner cell boundaries. As we have already mentioned, since we want to segment the inside of the cell, we try to construct initial segmentation function whose compact support does not exceed the border of the cell. We proceed as follows. Supposing that we have at disposal the approximate cell nuclei centers, we construct a function with a constant positive value (e.g. $u_0(x)=1$) inside a sphere centered in the detected center of the cell nucleus. Outside the sphere, we set $u_0(x)=0$. Then we let the function evolve according to the GSUBSURF model (14). In Fig. 8, we illustrate the process on several selected cells. We show the cell nuclei with the detected centers, after the corresponding cell membrane image with the initial segmentation function and finally the segmented inner cell boundaries. For this example, we set the following values of segmentation parameters: $K=1000$, $w_a=10.0$, $w_d=0.2$, $\varepsilon=10^{-3}$, $\sigma=0.0001$, $\tau_S=0.1$, $h_1=h_2=h_3=1.0$. The process is stopped when we do not observe any significant change of the segmented object.

The segmentation of the inner cell borders has several useful applications. Besides the extraction of the intercellular skeleton, it can be used, for example, to determine the inner volume of the cells (see Section 4.4). Another interesting application is the detection of mitoses (cell divisions). The idea is illustrated in Fig. 9. At a certain stage of the cell division (anaphase), the nucleus is already split in two parts while the whole cell is not divided yet. As a consequence, the center detection algorithm finds two centers in a single cell. After, if we start the segmentation from these two centers, we obtain very similar results.

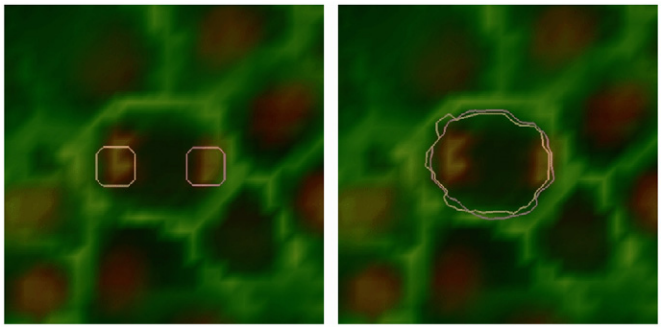

Fig. 9. Mitosis detection. On the left, we can see a 2D slice of data with nuclei (red) and membranes (green) superimposed and the initial segmentation functions corresponding to the centers of the two nuclei. On the right, the result of segmentation which is very similar for both centers. (For interpretation of the references to color in this figure legend, the reader is referred to the web version of this article.)

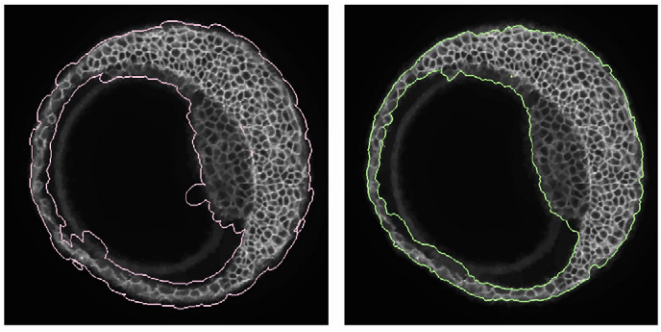

Fig. 10. Segmentation of the embryo surface. Left, the initial condition. Right, the segmentation result.

Therefore, by comparing the segmented objects belonging to different nuclei centers, the cell divisions can be easily located.

Remark 2. In the results presented in this paper, the segmentation of all cells was fully automatic except the epithelial (outermost) cells. The shape of these cells is specific, they are very flat and with dimensions several times larger than the dimensions of the inner cells. The quality of the data in this region can vary significantly, both the cell membranes and cell nuclei contain artifacts and unexpected structures. Therefore, the algorithms presented above as well as the center detection algorithm do not always provide results of sufficient quality. For this reason, the center detection in the epithelium was corrected manually and the cell segmentation was approximated by the following procedure. The size of each cell was estimated by the distance of its center to its nearest epithelial neighbor. Then the epithelial region was divided according to the Voronoi principle, taking in account

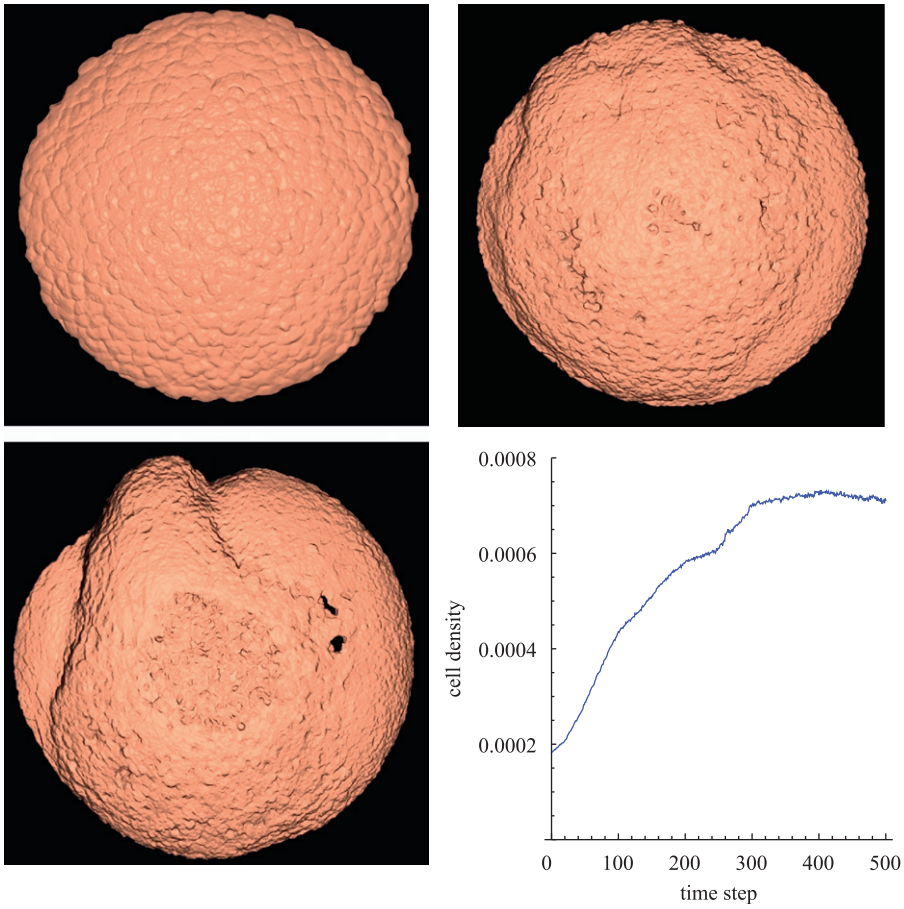

Fig. 11. Computation of the global cell density. Top and bottom left, segmented surface of the embryo at three different stages of the development. Bottom right, the plot of time evolution of the global cell density.

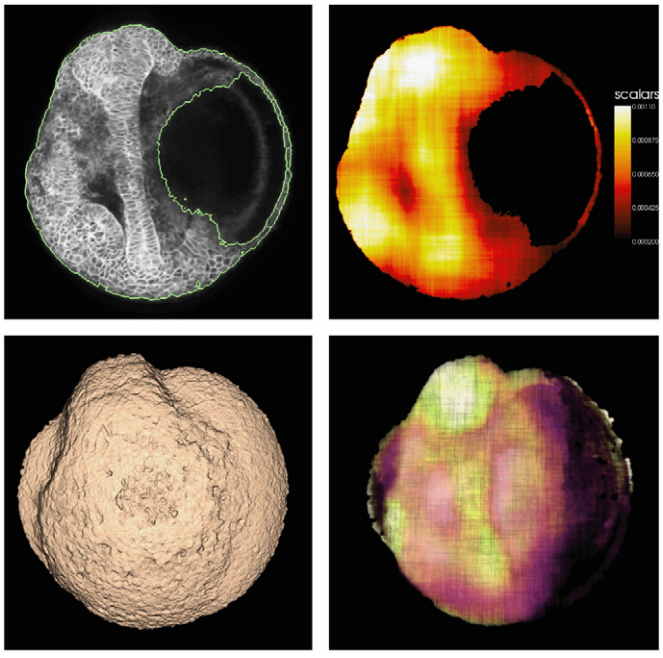

Fig. 12. Computation of the local cell density. Top left, 2D slice of the segmented embryo surface. Top right, the corresponding distribution of local cell density. Bottom left, segmented surface of the embryo in 3D view. Bottom right, the volume rendering of the local cell density with recognizable structures. Brighter colors correspond to higher local density. (For interpretation of the references to color in this figure legend, the reader is referred to the web version of this article.)

Table 5
The mean Hausdorff distance of the automatically segmented intercellular skeleton from the gold standard.

Cells	Min. MHD	Max. MHD	Mean MHD
37	0.482 μm	2.819 μm	0.939 μm

the approximate cell size. As the structure of epithelial cells is naturally similar to Voronoi tiling, this approach provides a sufficiently good approximation, see Fig. 18.

4.2. Segmentation of the embryo surface

In order to segment the surface, i.e. the outer border of the embryo, we have to construct the initial condition similar to the embryo shape. We proceed similarly as in the case of cell segmentation, i.e. for each cell, we set $u_0(x) = c > 0$ inside an ellipsoid centered in the detected nucleus center and $u_0(x) = 0$ outside. The difference is that this time the ellipsoids should overlap so that their union covers the whole visible part of the embryo. The ellipsoids are oriented in such a way that their longest diameter is approximately tangent to the surface of the embryo. In Fig. 10, we show such an initial segmentation function together with the segmentation result. This time we set $K=1000$, $w_a=10.0$, $w_d=2.0$, $\varepsilon = 10^{-3}$, $\sigma = 0.0001$, $\tau_S = 0.1$, $h_1 = h_2 = h_3 = 1.0$. The stopping time was $T_S=100$.

The segmentation of the surface of the embryo can be used to determine some quantitative characteristics of the developing

organism like its surface or volume. The center detection algorithm also provides the number of cells at each time step of the imaging and therefore we are also able to compute the global or local density of cells that can serve as useful criteria for comparing the evolution of two different individuals. Thus we can see e.g. the difference between organisms that develop in different conditions, for example when they are treated with a drug. In Fig. 11 we show the segmented surface of the embryo at three different stages of the development. Together with that, we provide a plot of the time evolution of the global cell density. Fig. 12 displays some local density results. The embryo is shown at an early stage of organogenesis and the forming brain, spinal chord and somites can be recognized in the membrane image as well as in the local density visualization.

4.3. Extraction of the intercellular skeleton

As we have already mentioned before, the intercellular skeleton is given by the ridges of the distance function to the segmented inner cell boundaries and by the embryo surface segmentation. Before we proceed to the results and practical applications, we provide a validation of the technique described in Section 3.3. For this purpose, we manually segmented a group of 37 cells – the 'gold standard' – so that we obtained their outer borders attached to each other (in order to do this, we used ITK Snap software tool [21]). After, we compared them with the automatically segmented skeleton. Such comparison validates not only the segmentation of the intercellular borders but indirectly the whole sequence of the described methods as the

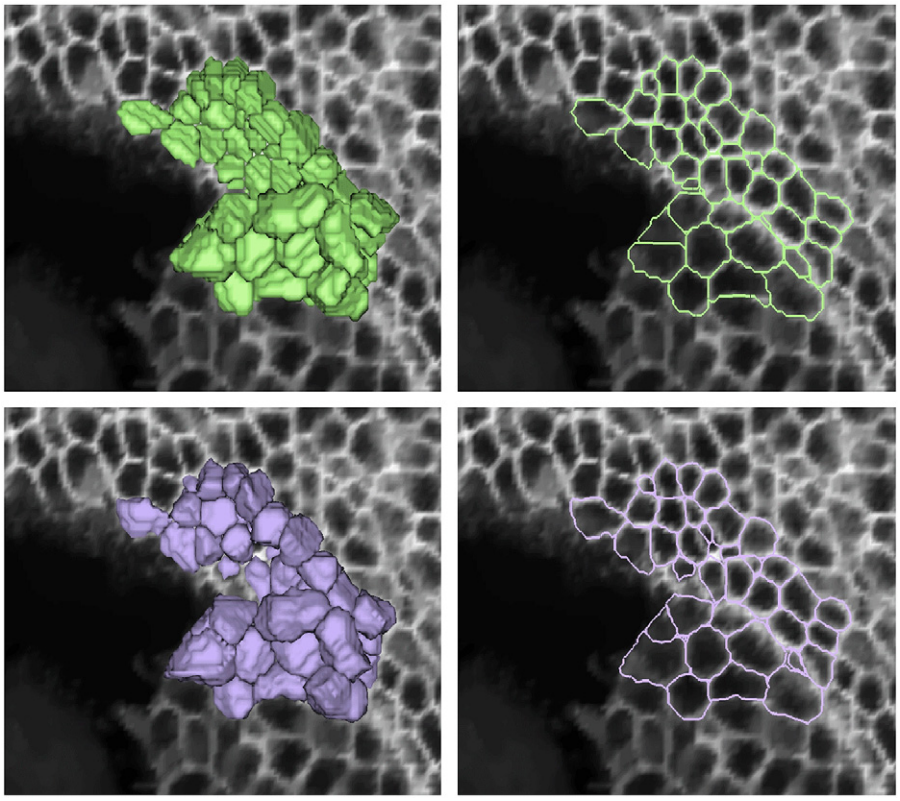

Fig. 13. Manually and automatically segmented outer cell boundaries. Top, the manual segmentation in 3D and 2D slice views. Bottom, the automatic segmentation.

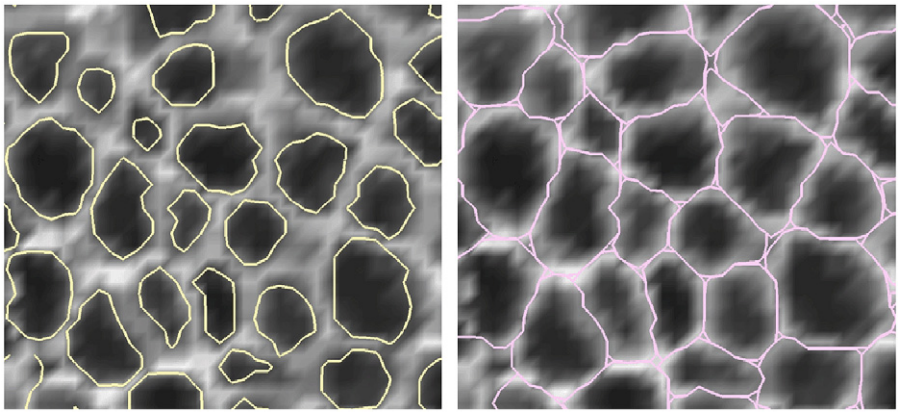

Fig. 14. A detail of the inner cell boundary segmentation (left) with the corresponding segmented intercellular skeleton (right).

final form of the intercellular skeleton depends on their results. We selected a group of cells where some cell borders coincide with the border of the embryo so that the global surface segmentation could be also partially validated.

The comparison is realized by computing the mean Hausdorff distance between the manually segmented objects and the objects obtained by automatic segmentation. Let $A=\{a_1,\ldots,a_p\}$ and $B=\{b_1,\ldots,b_q\}$ denote two finite point sets. Then the mean Hausdorff distance is defined as, cf. [23]

$$MHD(A,B)=\max(mhd(A,B),mhd(B,A)),$$

where

$$mhd(A,B)=1/p\sum_{i=1}^{p}\min_{b\in B}\|a_i-b\|$$

is the so called mean directed Hausdorff distance and $\|\cdot\|$ is an underlying norm (usually Euclidean). In our case the sets A and B are given by discrete points that form the surface of the gold standard and the isosurface of the segmentation function that represents the automatically segmented intercellular borders. The result of the test is displayed in Table 5 and Fig. 13. In order to be able to evaluate the quality of the automatic segmentation, let us note that standard dimensions of the cells are approximately 10−20 μm. The values of model parameters for this example were set as follows. For the computation of the signed distance function we set $h_D=1.0$, $\tau_D=0.\overline{3}$, $\varepsilon_2=10^{-10}$. Then we constructed the initial segmentation function for the advective level set equation. Similarly as in the case of the inner cell border segmentation, the compact support of the function was located inside a sphere, now centered in the center of mass of the corresponding inner cell boundary. The parameters of the advective level set model were $g(x)=-1/(1+d(x))$ ($d(x)$ being the computed approximation of the distance function), $\tau_A=0.03$, $h_A=1.0$.

In Fig. 14 we show a detail of the inner cell boundary segmentation and the corresponding intercellular skeleton. We used the same values of parameters as in the validation example. Fig. 15 displays a 2D slice of the complete intercellular skeleton of an embryo.

Having the intercellular skeleton, we can evaluate the shape of the individual cells. While at the beginning of the embryonic development all cells have the same or very similar shape, at later stages they start to differentiate, and the embryo undergoes morphogenesis by forming germ layers, recognizable structures and finally organs. Figs. 16–18 show several examples concerning the cell shapes. The chosen cell membrane image represents the late gastrulation period of the embryonic development when the organs are not yet formed but we can recognize several cell layers. The embryo is situated on a giant yolk cell and it is covered by a thin one-cell thick epithelial enveloping layer. The intermediate multilayer of cells, the blastoderm, consists of two parts – the epiblast (future skin and neural tissues) and the hypoblast (future muscles, bones, blood, digestive and respiratory organs, etc.), see Fig. 16. Fig. 17 demonstrates automatic recognition of the cell shapes. According to [10], the epiblast consists of a pseudostratified epithelium. Here we rather identify it as a multilayered structure. The cells of the inner epiblast tend to be elongated and oriented in the radial direction with respect to the embryo surface. This makes them distinguishable from the outer epiblast cells that do not show the elongation in the radial direction and form a single layer. The epiblast can be distinguished from the hypoblast and a thick border separates the two

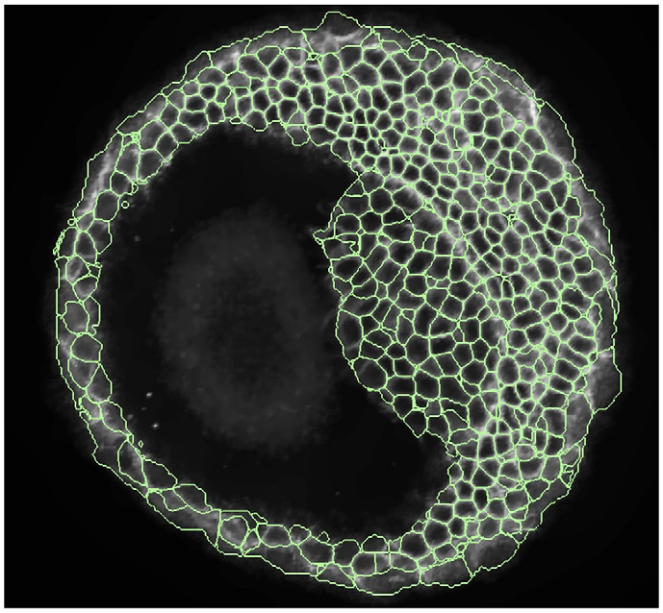

Fig. 15. 2D slice of the complete intercellular skeleton.

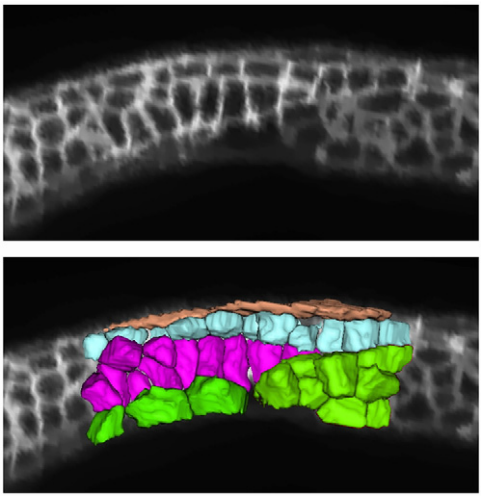

Fig. 16. A 2D slice of data with differentiated cell layers and a selection of automatically segmented cells corresponding to these layers. From the top: epithelium, exterior epiblast, interior epiblast and hypoblast.

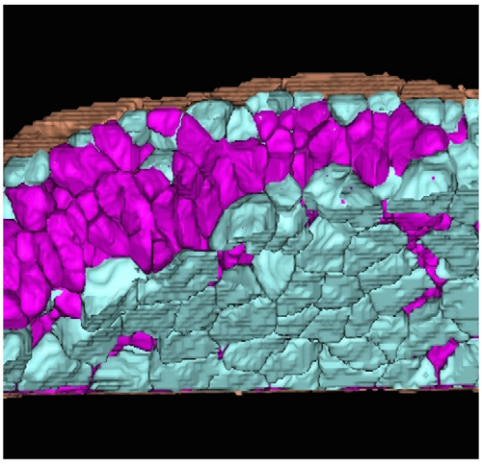

Fig. 17. Automatic recognition of the cell shapes. From the top: epithelium, exterior epiblast, interior epiblast and hypoblast enveloping cells. The interior epiblast cells are more elongated and oriented in the radial direction with respect to the embryo surface, contrarily to the exterior epiblast cells and the hypoblast enveloping cells.

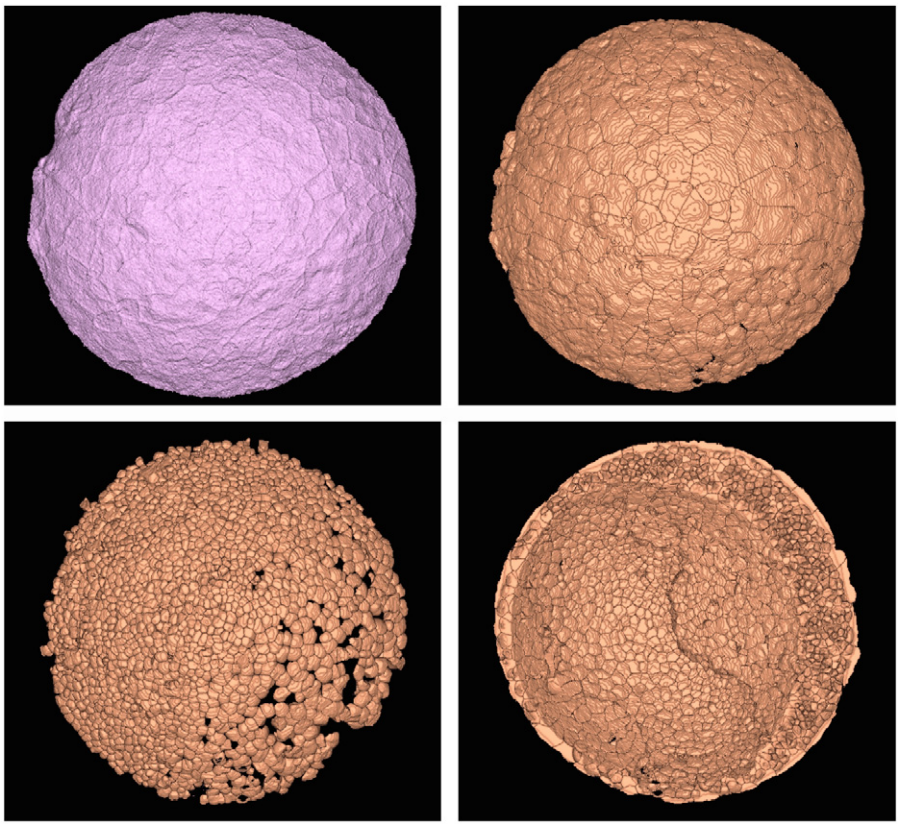

Fig. 18. Visualization of the embryo cell layers. Top left, the isosurface $I=20$ of the cell membrane image. Top right, the approximation of the corresponding epithelial cells segmentation. Bottom left, the exterior epiblast cells. Bottom right, the cells of the embryo viewed from the inside of the yolk cell. We can observe thickening of the blastoderm on the right side—the embryonic shield. Later on, the spine will be formed along its symmetry axis.

Table 6
Quantitative characteristics of the embryo.

Number of cells	3919
Number of epithelial cells	181
Outer embryo surface	4.24*e*5 μm^2
Embryo volume	8.29*e*6 μm^3
Average cell volume (inner cells)	842.3 μm^3
Global cell density	4.73*e*−4 cells/μm^3
Cell contact surface	1.62*e*6 μm^2

germ layers that are sliding on each other. The cell shape and its orientation can be determined according to the shape of its bounding box [20]. Fig. 18 shows various views of the embryo and its cell layers.

4.4. Quantitative characteristics of the embryo

Finally, we computed several quantitative characteristics of the embryo and its cells for a chosen 3D image displayed in Fig. 1. This image represents the stage of embryonic development approximately 9 h after fertilization and the embryo is about to complete the gastrulation. The 3D image dimensions are $512 \times 512 \times 100$ voxels while one voxel represents a cube with side length 1.51 μm. The quantitative characteristics that we calculated are listed in Table 6. The volume and surface of the embryo and of the individual cells were computed using VTK libraries [18], particularly the vtkMassProperties class. By cell volume we mean the inner volume. If we denote by S_e the surface of the embryo and by S_c the sum of the surfaces of all cells, we can compute the area of the cell contact surface S_{ccs} as

$$S_{ccs} = \frac{S_c - S_e}{2}.$$

The outer surface of the embryo is approximated by $S_{epith}/2$, where S_{epith} is the sum of the surface of the epithelial cells. Here we take advantage of the fact that the epithelial cells are very flat compared with the other cells and we neglect their thickness.

Conflict of interest statement

None declared.

Acknowledgment

This work was supported by the grant VEGA 1/0733/10.

References

[1] P. Bourgine, R. Čunderlík, O. Drblíková-Stašová, K. Mikula, N. Peyriéras, M. Remešíková, B. Rizzi, A. Sarti, 4D embryogenesis image analysis using PDE methods of image processing, Kybernetika 46 (2) (2010).
[2] P. Bourgine, P. Frolkovič, K. Mikula, N. Peyriéras, M. Remešíková, Extraction of the intercellular skeleton from 2D microscope images of early embryogenesis, in: Lecture Notes in Computer Science, Proceeding of the 2nd International Conference on Scale Space and Variational Methods in Computer Vision, Voss, Norway, June 2009, vol. 5567, Springer, 2009, pp. 38–49.
[3] V. Caselles, R. Kimmel, G. Sapiro, Geodesic active contours, International Journal of Computer Vision 22 (1997) 61–79.
[4] Y. Chen, B.C. Vemuri, L. Wang, Image denoising and segmentation via nonlinear diffusion, Computers and Mathematics with Applications 39 (2000) 131–149.

[5] M. Campana, B. Maury, P. Dutreix, N. Peyriéras, A. Sarti, Methods toward in vivo measurement of zebrafish epithelial and deep cell proliferation, Computer Methods and Programs in Biomedicine 98 (2) (2010) 103–117.
[6] S. Corsaro, K. Mikula, A. Sarti, F. Sgallari, Semi-implicit co-volume method in 3D image segmentation, SIAM Journal on Scientific Computing 28 (6) (2006) 2248–2265.
[7] O. Drblíková, K. Mikula, N. Peyriéras, The nonlinear tensor diffusion in segmentation of meaningful biological structures from image sequences of zebrafish embryogenesis, in: Lecture Notes in Computer Science, Proceeding of the 2nd International Conference on Scale Space and Variational Methods in Computer Vision, Voss, Norway, June 2009, vol. 5567, Springer, 2009, pp. 63–74.
[8] P. Frolkovič, K. Mikula, Flux-based level set method: a finite volume method for evolving interfaces, Applied Numerical Mathematics 57 (4) (2007) 436–454.
[9] P. Frolkovič, K. Mikula, N. Peyriéras, A. Sarti, A counting number of cells and cell segmentation using advection-diffusion equations, Kybernetika 43 (6) (2007) 817–829.
[10] C.B. Kimmel, W.W. Ballard, S.R. Kimmel, B. Ullmann, T.F. Schilling, Stages of embryonic development of the zebrafish, Developmental Dynamics 203 (1995) 253–310.
[11] S. Kichenassamy, A. Kumar, P. Olver, A. Tannenbaum, A. Yezzi, Conformal curvature flows: from phase transitions to active vision, Archive for Rational Mechanics and Analysis 134 (1996) 275–301.
[12] Z. Krivá, K. Mikula, N. Peyriéras, B. Rizzi, A. Sarti, O. Stašová, Zebrafish early embryogenesis 3D image filtering by nonlinear partial differential equations, Medical Image Analysis 14 (4) (2010) 510–526.
[13] K. Mikula, N. Peyriéras, M. Remešíková, A. Sarti, 3D embryogenesis image segmentation by the generalized subjective surface method using the finite volume technique, in: Proceedings of FVCA5—5th international symposium on finite volumes for complex applications, Hermes Publication, Paris, 2008.
[14] K. Mikula, M. Remešíková, Finite volume schemes for the generalized subjective surface equation in image segmentation, Kybernetika 45 (4) (2009).
[15] E. Rouy, A. Tourin, Viscosity solutions approach to shape-from-shading, SIAM Journal on Numerical Analysis 29 (3) (1992) 867–884.
[16] A. Sarti, R. Malladi, J.A. Sethian, Subjective surfaces: a method for completing missing boundaries, Proceedings of the National Academy of Sciences of the United States of America 12 (97) (2000) 6258–6263.
[17] A. Sarti, C. Ortiz, S. Locket, R. Malladi, A geometric model for 3D confocal image analysis, IEEE Transactions on Biomedical Engineering 47 (12) (2000) 1600–1610.
[18] W. Schroeder, K. Martin, B. Lorensen, Visualization Toolkit, Kitware Inc., 2004.
[19] J.A. Sethian, Level Set Methods and Fast Marching Methods: evolving Interfaces in Computational Geometry Fluid Mechanics, Computer Vision, and Material Science, Cambridge University Press, New York, 1999.
[20] O. Tassy, F. Daian, C. Hudson, V. Bertrandt, P. Lemaire, A quantitative approach to the study of the cell shapes and interactions during early chordate embryogenesis, Current Biology 16 (2006) 345–358.
[21] P.A. Yushkevich, J. Piven, H. Cody Hazlett, R. Gimpel Smith, S. Ho, J.C. Gee, G. Gerig, User-guided 3D active contour segmentation of anatomical structures: significantly improved efficiency and reliability, Neuroimage 31 (3) (2006) 1116–1128.
[22] C. Zanella, M. Campana, B. Rizzi, C. Melani, G. Sanguinetti, P. Bourgine, K. Mikula, N. Peyriéras, A. Sarti, Cells segmentation from 3-D confocal images of early zebrafish embryogenesis, IEEE Transactions on Image Processing 19 (2) (2010).
[23] J.W. Zhang, G.Q. Han, Y. Wo, Image registration based on generalized and mean Hausdorff distances, in: Proceedings of the Fourth International Conference on Machine Learning and Cybernetics, Guangzhou, 2005.
[24] H.-K. Zhao, Fast sweeping method for eikonal equations, Mathematics of Computation 74 (2005) 603–627.
[25] H.-K. Zhao, S. Osher, R. Fedkiw, Fast surface reconstruction using the level set method, in: Proceedings of IEEE Workshop on Variational and Level Set Methods – VLSM'01, Vancouver, 2001, pp. 194–201.